Check for updates

Cascaded utilization of magnetite nanoparticles@onion-like carbons from wastewater purification to supercapacitive energy storage†

Xin Jiao,[a,b,c,d,e] Min Xiao,[a,b,c,d] Fengshi Cai,[a,b,c,d] Yingchun Fan,[a,b,c,d] Shuaipeng Meng,[a,b,c,d] Xiude Guan,[e] Huiquan Wang[a,b,c,d] and Chenguang Zhang (ID) *[a,b,c,d]

Developing high-performance carbon-based materials for environmental and energy-related applications produces solid waste with secondary pollution to the environment at the end of their service lives. It is still challenging to utilize these functional materials in a sustainable manner in different fields. In this study, we demonstrate a cascaded utilization of an Fe_3O_4@onion-like carbon (Fe_3O_4@OLC) structure from waste-water adsorbents to a supercapacitor electrode. The structure was formed by carbonizing Fe_3O_4@oleic acid monodisperse nanoparticles into interconnected Fe_3O_4@OLCs and subsequent insufficient acid etching. The hollow OLCs in the outside region of the hybrid structure provide high surface area and the encapsulated Fe_3O_4 nanoparticles in the inside region offer high ferromagnetism. The three-dimensionally interconnected graphitic layers are advantageous for efficient separation and high conductivity. As a result, the maximum saturation adsorption capacity of insufficiently etched interconnected Fe_3O_4@OLCs can reach up to 90.2 mg g^{-1} and they can be efficiently separated under a magnetic field. Furthermore, the hybrid structure is thermally transformed into N-doped HOLCs, which are demonstrated to be a high-performance supercapacitor electrode with high specific capacitance and high electrochemical stability. The cascaded utilization of the hybrid structure in this study is meaningful for eco-friendly development of functional materials for environmental and energy storage applications.

1. Introduction

The environmental pollution and energy crisis are major global issues that endanger human survival and obstruct the development of a safe society.[1] It is essential to solve energy and environmental issues through emerging technologies based on materials science. Since the industrial revolution, human activities associated with materials and energy have been consistently accompanied by augmented waste and scat-tered emissions. People have realized that this early utilization method of materials is unsustainable, leading to an emphasis on responsibilities for recycling products through legislative measures.[2] A comprehensive industrial chain and corres-ponding industrial ecology including materials production and recycling have been developed. Reducing waste emissions and recycling materials can effectively address environmental issues, yet reusing waste produced in the early phases of the industrial chain tends to offer greater environmental benefits.[3]

Cascaded utilization of materials resources is commonly believed to be one of the effective methods to prolong materials lifecycles, enhance industrial ecology, and optimize both economic and environmental benefits. The goal of cas-caded utilization is to delay the inevitable end-point (like energy recovery and landfilling) by retaining products or materials at higher levels for an extended period, that is, extending their lifecycle by using them in various applications, which conforms to the concept of a circular economy.[3,4] Although various functional nanomaterials have been devel-oped for the environmental and energy-related applications with high performances in specific areas, yet high-value-added

[a]*School of Materials Science and Engineering, Tianjin University of Technology, Tianjin 300384, PR China. E-mail: cgzhang@tjut.edu.cn*
[b]*Institute for Green Nanotechnology, Tianjin University of Technology, Tianjin 300384, PR China*
[c]*Tianjin Key Laboratory for Photoelectric Materials & Devices, Tianjin University of Technology, Tianjin 300384, PR China*
[d]*Key Laboratory of Display Materials and Photoelectric Devices, Tianjin University of Technology, Ministry of Education, Tianjin 300384, PR China*
[e]*College of Materials Engineering, Shanxi College of Technology, Shuozhou, Shanxi Province 036000, PR China*
†Electronic supplementary information (ESI) available. See DOI: https://doi.org/10.1039/d4dt02559h

cascaded utilization of these materials in their later life cycles is rarely considered. There is a need to design reasonable cascaded utilization schemes based on materials advantages to maximize their environmental and economic benefits. Therefore, developing functional materials for energy/environmental applications and devising reasonable waste recycling pathways are important for improving the industrial ecology of materials and the sustainability of resource utilization.

Organic dyes are widely used in many areas such as textile, papermaking, leather and printing.[5] Nevertheless, organic dyes in industrial wastewater have become one of the major hazardous industrial pollutants, causing serious health and safety problems in human beings and the environmental ecosystem.[6] Adsorption is currently a widely adopted and reliable method for removing organic pollutants from wastewater.[7] Common adsorbents, including carbon materials, zeolite, montmorillonite and kaolinite, have been reported for contaminant removal.[8,9] Spent adsorbents are typically disposed by incineration and landfilling, which not only adds disposal costs but also poses potential risks of secondary pollution. Therefore, from the perspective of the long lifecycle of adsorption materials, the recovery and sustainable management of spent adsorbents are important.[10] A primary practical challenge lies in the efficient recycling, harmless processing, and high-value-added application of waste adsorbents, necessitating the urgent development of high-performance, easily separable adsorbent materials and feasible ways for their cascaded utilization.[11,12]

The initial step in recycling is separating the spent adsorbents from waste water. Various technologies, such as precipitation, filtration,[13] centrifugation,[14] and magnetic separation,[15] have already been used for separating and recovering spent adsorbents. Among these methods, magnetic separation is considered as an efficient technique with operational simplicity and high efficiency. Magnetite nanoparticles (Fe_3O_4 NPs) have widely attracted interest as efficient adsorbents in research and industrial fields due to their advantages of easy separation in an external magnetic field, high surface area, low-toxicity and reusability.[16] However, Fe_3O_4 NPs tend to agglomerate, reducing the available surface area for adsorption.[17] Moreover, they can be easily oxidized in open air or etched in acidic medium. These disadvantages lead to low adsorption capabilities of Fe_3O_4 NPs. Compositing Fe_3O_4 NPs with carbon materials, such as activated carbon, biochar, graphitic carbon nitride, and reduced graphene oxide, is considered as an effective strategy to improve the stability and dispersity of nanoparticles.[18–20] For example, an Fe_3O_4/activated carbon composite synthesized by a diol thermal decomposition process shows high adsorption efficiency for removing rhodamine B and methyl orange from wastewater.[21] A magnetic graphene nanocomposite (Fe_3O_4/G) prepared by a solvothermal method can efficiently remove methylene blue (MB) from wastewater.[22] An Fe_3O_4/carbon nanotube (CNT) composite formed by grafting Fe_3O_4 particles onto CNTs has a good ability to capture pesticides and bisphenol A in wastewater.[23,24] However, the Fe_3O_4 NPs in these studies were formed without a carbon coating, and suffer from instability when exposed to open air or an acidic environment during long-term use. Moreover, aggregation and exfoliation can easily occur on these Fe_3O_4 NPs, leading to failure during treatment. Although core–shell Fe_3O_4@C structures have been prepared to solve these problems,[25–28] the thick carbon coatings and inhomogeneous size of Fe_3O_4 NPs can suppress the ferromagnetism and reduce the surface area. Therefore, it is of great importance to develop an Fe_3O_4@C hybrid structure to overcome these challenges for realizing high-efficiency water treatment.

Although magnetic adsorbents can undergo multiple cycles of reuse after adsorbing dyes through recovery and cleaning processes, the end adsorption products are typically treated as solid waste, which adds to secondary pollution risks to the environment. Therefore, it is equally important to achieve harmless treatment of the adsorbents. Techniques of desorption, photodegradation, and biodegradation have been developed for adsorbed pollutants, aiming at the regeneration and detoxification of the spent adsorbents,[29,30] including thermal degradation,[31] solvent washing regeneration,[32] microwave irradiation,[33] supercritical fluid regeneration,[34] advanced oxidation processes,[35] and microbial-assisted degradation.[36] Although products after degradation treatment exhibit low environmental toxicity, they do not contribute to added economic value. The cascaded utilization for creating high-value-added products can notably improve economic and resource recovery efficiency. A carbon-based supercapacitor, with high energy density and excellent power density, is a highly efficient energy storage device for fast storing/releasing of large amount of energy. Heteroatom-doped porous carbons have been reported as high-performance supercapacitor electrode materials. Given the rich presence of elements O/N/S in organic dyes, they are expected to serve as precursors for creating heteroatom-doped carbon structures. Hence, it is meaningful to develop appropriate techniques to transform waste adsorption products into valuable supercapacitor electrode materials for realizing the cascaded utilization of carbon-based nanomaterials in the areas of dye adsorption and energy storage.

Herein, we present an interconnected onion-like carbon (OLC) structure with encapsulated magnetic nanoparticles incompletely removed, realizing a cascaded utilization from wastewater purification adsorbents to supercapacitor electrode materials. The hybrid structure was prepared by carbonizing the Fe_3O_4@oleic acid monodisperse nanoparticles into interconnected Fe_3O_4@OLCs and subsequent insufficient acid etching of the inner Fe_3O_4, which renders the hybrid structure with hollow OLCs in the outer part and remnant Fe_3O_4 nanoparticles encapsulated OLCs in the inside part. The hybrid structure exhibits high adsorption capacity and good recyclability as adsorbents for removing methylene blue (MB). Furthermore, the recycled MB-adsorbed Fe_3O_4@OLCs were transformed into N-doped hollow onion-like carbon (HOLC) through a thermal process, which achieves high performances as supercapacitor electrode materials. This study provides a structural design for efficient organic contaminant removal,

and also demonstrates that the organic dye-adsorbed carbon structure can be converted into a supercapacitor electrode with good energy storage performances. The Fe_3O_4@OLC hybrid structure developed in this study holds promise as a novel functional material in applications in the fields of environmental pollution and energy storage in a cascaded utilization manner.

2. Experimental

2.1. Materials

All chemicals in the experiment were used as received. γ-Fe_2O_3 (AR) was purchased from Shanghai McLin Biochemical Co., Ltd. Oleic acid (99%, AR) and 1-octadecene (>90.0%, GC) were purchased from Sigma Aldrich. *n*-Hexane and ethanol were purchased from Tianjin University Kuwait Chemical Co., Ltd. Methylene blue (AR) was purchased from Tianjin Bodi Chemical Co., Ltd.

2.2. Synthesis of insufficiently etched interconnected Fe_3O_4@OLCs

Synthesis of Fe_3O_4@OA colloidal nanocrystals

Firstly, γ-Fe_2O_3 (0.356 g), oleic acid (2.260 g) and 1-octadecene (5 g) were mixed and stirred in a reactor with N_2 flow. Then, the mixture was heated at 120 °C for 30 min to remove residual water. Then the mixture was heated at 220 °C for 30 min to initiate the nucleation process of Fe_3O_4 nanocrystals, followed by heating at 320 °C for 30 min to start the growth process of Fe_3O_4@OA nanocrystals. After cooling to room temperature, ethanol and *n*-hexane were used to precipitate the Fe_3O_4@OA nanocrystals and remove the excess solvent and ligands by repeated centrifugation and purification. Finally, monodisperse Fe_3O_4@OA colloidal nanoparticles were dispersed in *n*-hexane and stored. Meanwhile, Fe_3O_4@OA nanocrystals with average particle sizes of 9.9 and 12.6 nm were obtained by the same process as described above, except that the amounts of OA added were 3.38 g and 4.62 g, respectively.

Preparation of interconnected Fe_3O_4@OLCs and insufficiently etched interconnected Fe_3O_4@OLCs

The *n*-hexane dispersion of Fe_3O_4@OA nanoparticles was concentrated at 90 °C for 4 h. During this period, the evaporation of *n*-hexane induced the self-assembly of the monodisperse Fe_3O_4@OA nanoparticles, which made the adjacent Fe_3O_4@OA nanoparticles come in tight contact to produce a continuous distribution of OA ligands. Then the OA was *in situ* transformed into covalently interconnected OLCs by heating at 500 °C for 2.5 h in Ar to obtain the Fe_3O_4@OLCs sample. Subsequently, the Fe_3O_4@OLC powder was immersed in a 1 M HCl aqueous solution (adding 0.5 g of Fe_3O_4@OLC powder to every 200 mL of HCl solution) and stirred at room temperature for 1 h to undergo etching. In this process, the difference in HCl permeability leads to the removal or retention of Fe_3O_4 in different regions of the material. The external Fe_3O_4 nanoparticles were etched, creating a hollow OLC structure, and the

internal Fe_3O_4 nanoparticles that were less accessible to the acid remained intact. The etched powder was ultimately rinsed with deionized water until it reached a neutral pH, and then dried at 60 °C for 5 h to produce insufficiently etched interconnected Fe_3O_4@OLCs.

2.3. Characterization

Transmission electron microscopy (TEM) was used to observe the morphology of Fe_3O_4@OA NPs and Fe_3O_4@OLCs (TECNAI G2 Spirit, FEI, OR, USA) at an accelerating voltage of 200 kV. X-ray diffraction (XRD) characterization was performed to analyze the crystalline structure of Fe_3O_4@OLCs using a diffractometer (SmartLab, Tokyo, Japan) with Cu Kα radiation at a sweeping rate of 10° min^{-1} and a range of 10–80°. Graphitization of insufficiently etched interconnected Fe_3O_4@OLCs was investigated using an Aberration-Corrected Czerny Turner Total Reflectance Raman spectrometer (HORIBA EVOLUTION, Paris, France) at a 532 nm laser excitation wavelength. A PerkinElmer STA 6000 spectrometer (Waltham, MA, USA) was used to collect Fourier transform infrared (FT-IR) spectra of Fe_3O_4@OA and Fe_3O_4@OLC samples. A vibrating sample magnetometer (VSM, Lakeshore-7404) was used to analyze the magnetic properties. Thermogravimetric analysis (TGA) was conducted on a TG-DSC analyzer (SDT650, TA, Waters, USA). The structure of the elemental states of the insufficiently etched interconnected Fe_3O_4@OLC hybrid structure was examined using an X-ray photoelectron spectroscopy (XPS) setup (ESCALAB250Xi, Waltham, MA, USA) equipped with a monochromatic Al-Kα radiation source (photon energy = 1486.6 eV) as the excitation source, operated at a base pressure of $\sim 5 \times 10^{-10}$ mbar. The adsorption performance of insufficiently etched interconnected Fe_3O_4@OLCs to MB was characterized using a UV-vis-near-IR spectrophotometer (TU-1901, PUXI Co. Ltd, Beijing, China). The electrochemical performances of all samples were measured using an electrochemical workstation (CHI 660E). The electrochemical impedance spectroscopy (EIS) spectra were recorded in a frequency range of 10^{-1} Hz to 10^5 Hz with an AC amplitude of 5 mV.

2.4. Adsorption experiments

The batch adsorption experiment was conducted by mixing the insufficiently etched interconnected Fe_3O_4@OLC adsorbent and MB dye in a beaker by stirring at 200 r min^{-1}, from which the liquid sample was taken out for measurement every 10 min. To study the adsorption isotherms, insufficiently etched interconnected Fe_3O_4@OLCs (4 mg) with different initial concentrations (5, 10, and 15 mg L^{-1}) were put into 20 mL of MB solution. The adsorption performance of the insufficiently etched interconnected Fe_3O_4@OLCs was quantitatively evaluated by *operando* monitoring of the MB content in water using the UV-vis spectrophotometer.

The adsorption capacity q (mg g^{-1}) of Fe_3O_4@OLCs was evaluated using eqn (1):

$$q = (C_0 - C_e)/m \times V \tag{1}$$

where C_0 and C_e are the original and equilibrium concentrations (mg L^{-1}) of MB solution, respectively; m (g) is the added amount of insufficiently etched interconnected Fe$_3$O$_4$@OLCs adsorbent; and V (L) is the solution volume.

According to the Langmuir model of eqn (2) and Freundlich model of eqn (3), the adsorption isotherm was fitted to determine the adsorption mechanism of insufficiently etched interconnected Fe$_3$O$_4$@OLCs:

$$q_e = (q_m K_L C_e)/(1 + K_L C_e) \qquad (2)$$

$$q_e = K_F(C_e)^{(1/n)} \qquad (3)$$

where C_e represents the equilibrium adsorption concentration (mg L^{-1}); q_m represents monolayer adsorption efficiency (mg g^{-1}); K_L represents the adsorption constant (L g^{-1}); K_F represents the coefficient of adsorption capacity (L g^{-1}); and n represents the adsorption strength.

3. Results and discussion

Fig. 1 shows the preparation process of the hybrid structure of interconnected OLCs with encapsulated Fe$_3$O$_4$ incompletely removed. The monodisperse Fe$_3$O$_4$@OA nanocrystals with a uniform size distribution were synthesized through a colloidal chemical process. The mixture of maghemite (γ-Fe$_2$O$_3$) and excess oleic acid (OA) can generate a large number of iron–oleate complexes as precursors. The Fe$_3$O$_4$ nanocrystals were then obtained by thermal decomposition of the complexes in 1-octadecene solvent with a high-boiling-point.[24] Instead of employing toxic and expensive iron pentacarbonyl as a raw material, this process employs γ-Fe$_2$O$_3$ with the advantages of easy and inexpensive acquisition from nature to generate an iron–OA complex for subsequent thermal decomposition. During the thermal decomposition process of the iron–oleate complex at 220 °C, one OA ligand is dissociated from the iron–oleate complex by CO$_2$ elimination, which initiates a homogeneous nucleation process.[37,38] Subsequently, the dissociation of the remaining OA ligands at 320 °C further promoted the growth of nanocrystals. As shown in Fig. 2a–c, the Fe$_3$O$_4$@OA nanocrystals have rather uniform size distributions, and the nanoparticle size can be controlled by adjusting the adding amount of OA. When the molar ratios of OA to γ-Fe$_2$O$_3$ were 4 : 1, 5 : 1 and 6 : 1, Fe$_3$O$_4$@OA nanoparticles with an average particle size of 5.6, 9.9 and 12.6 nm, respectively, were obtained. The presence of a large number of precursor monomers in the reaction system at the initial stage of the nucleation process without obvious direction selection led to the growth of spherical Fe$_3$O$_4$ nanoparticles.[39]

The hexane solvent evaporation during the thermal treatment triggered the self-assembly of Fe$_3$O$_4$@OA nanoparticles, resulting in the formation of a continuously distributed OA framework among adjacent nanoparticles. Then Fe$_3$O$_4$@OA nanoparticles were carbonized at 500 °C to form the Fe$_3$O$_4$@OLC hybrid structure (Fig. 1). In the early stage of the carbonization process, non-graphitic species can be generated on the surface of Fe$_3$O$_4$ nanoparticles due to the incomplete decomposition of OA molecules. At relatively low temperatures,

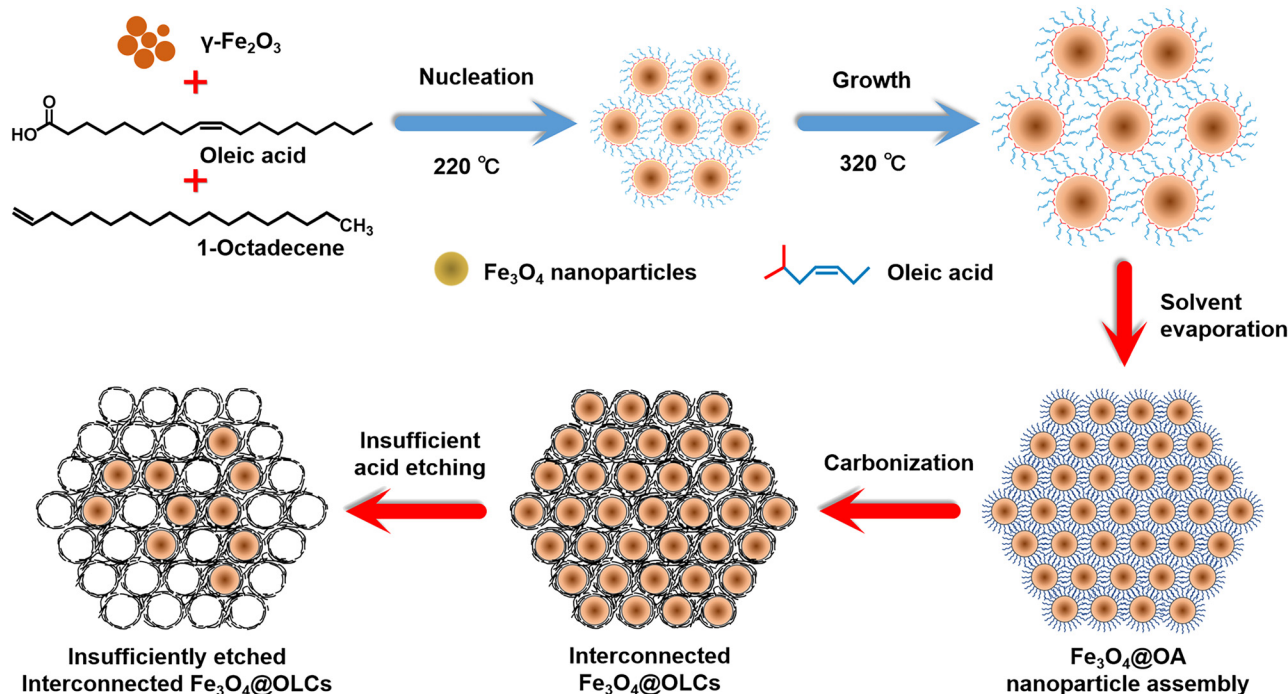**Fig. 1** Schematic illustration of the synthesis process of the monodisperse Fe$_3$O$_4$@OA colloidal nanocrystals and insufficiently etched interconnected Fe$_3$O$_4$@OLCs.
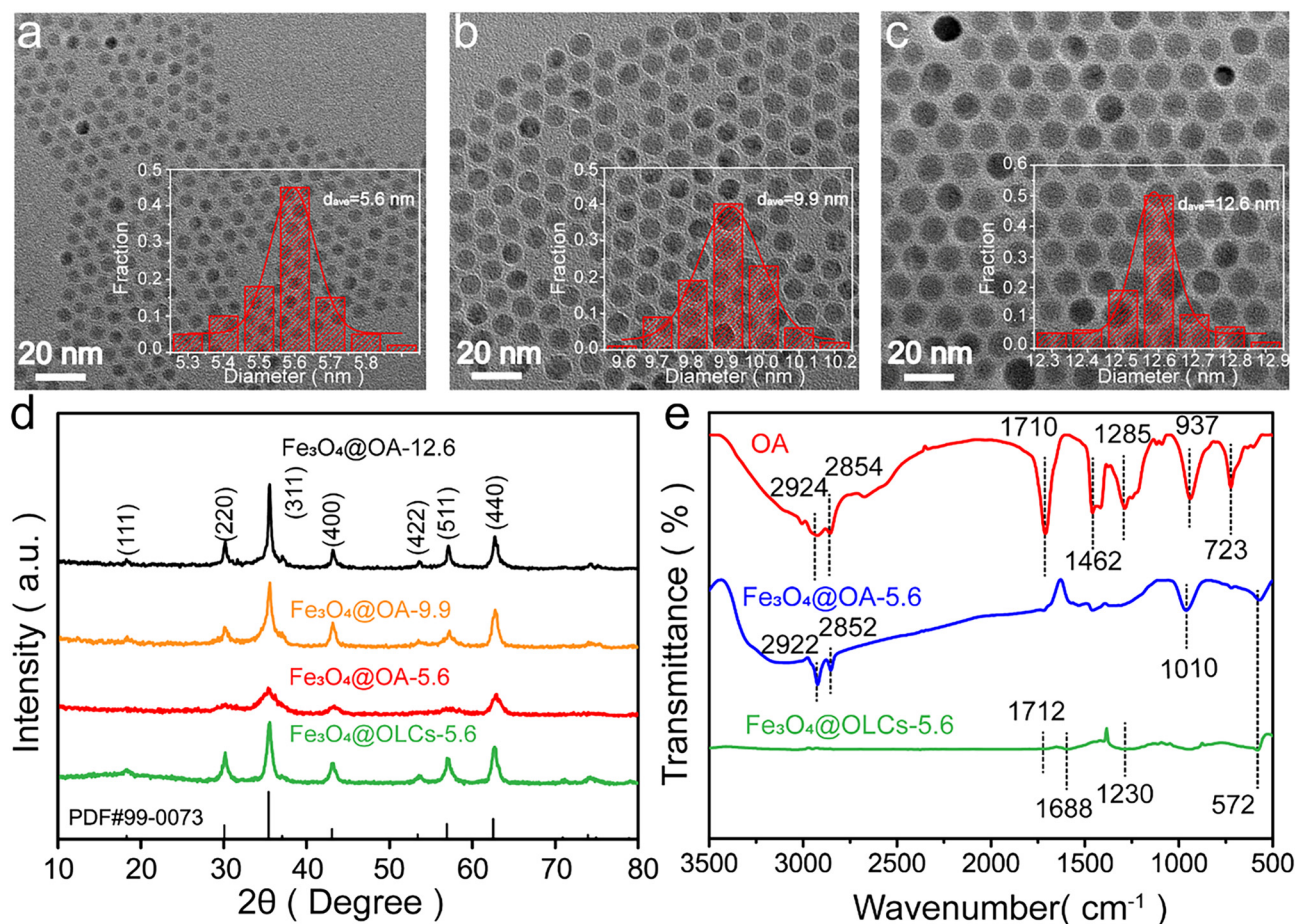
Fig. 2 TEM images of monodisperse Fe_3O_4@OA nanoparticles with different average sizes of (a) 5.6 nm, (b) 9.9 nm, and (c) 12.6 nm. Insets in (a–c) show particle size distribution histograms. (d) XRD profiles of Fe_3O_4@OA nanoparticles and interconnected Fe_3O_4@OLCs. (e) FT-IR spectra of OA, Fe_3O_4@OA, and interconnected Fe_3O_4@OLCs.

catalytic graphitization can be induced by Fe_3O_4 nanoparticles,[40] which can assist in the transformation of non-graphitized carbon species into partially graphitized carbon coatings and then more ordered graphitized layers at 500 °C. This process leads to the formation of three-dimensional covalently interconnected graphitic layers in the entire hybrid structure with monodisperse Fe_3O_4 nanoparticles encapsulated. Then the Fe_3O_4@OLCs were immersed in 1 M hydrochloric acid solution for 1 h to conduct an insufficient acid etching. HCl molecules etch away the Fe_3O_4 nanoparticles from outside into the inside part of the interconnected Fe_3O_4@OLC structure. The Fe_3O_4 nanoparticles in the outer part of the hybrid structure were dissolved and removed first due to the presence of defects on the graphitic shells, while the encapsulated Fe_3O_4 nanoparticles in the inside part of the hybrid structure still remained intact due to the poor permeability of HCl molecules into the inside part during such a short period of acid etching, which resulted in the formation of the Fe_3O_4@OLC hybrid structure with encapsulated Fe_3O_4 incompletely removed (Fig. 1). This preparation strategy can not only increase the specific surface area of the hybrid structure but also preserve

the ferromagnetism originating from the inner intact Fe_3O_4 nanoparticles, which is advantageous for use as efficient adsorbents for wastewater treatment and subsequent efficient magnetic field-induced separation.

The OA ligands on the surface of Fe_3O_4 serve as stabilizers to prevent the agglomeration of Fe_3O_4@OA nanocrystals (Fig. 2a–c). The terminating functional groups of OA ligands outwards are hydrophobic, rendering a good monodispersity in non-polar *n*-hexane solvent. The ~2 nm spacing between Fe_3O_4 nanoparticles corresponds to the length of the OA molecular chain, suggesting a monolayer of OA coating, which is essential for the subsequent formation of ultra-thin interconnected graphite coatings. XRD results (Fig. 2d) show typical diffraction peaks at 2θ = 30.1°, 35.5°, 43.2°, 54.2°, 57.1° and 62.7° that are assigned to the (220), (311), (400), (422), (511), and (440) crystal planes of the inverse-spinel type Fe_3O_4 structure (PDF#99-0073), respectively. After carbonization treatment, the peak position assigned to Fe_3O_4 nanocrystals does not change, suggesting that the heat treatment process at 500 °C did not cause the phase transition of Fe_3O_4 nanocrystals. It is found that the Fe_3O_4@OLCs have a wide peak signal

in the peak position range of $2\theta = 15–20°$, which originates from the partially ordered graphitic structures of OLCs obtained by low-temperature heat treatment.[41] Fourier transform infrared (FT-IR) characterization was carried out on the OA and Fe_3O_4@OA nanoparticles before and after heat treatment (Fig. 2e). In the spectrum of Fe_3O-@OA nanoparticles, the bands at 2924 cm^{-1} and 2854 cm^{-1} are attributed to the asymmetric and symmetric stretching of $-CH_3$ and $-CH_2-$ in OA, respectively. The band at 1710 cm^{-1} is derived from the asymmetric vibrations of unidentate carboxylate, and the band at 1285 cm^{-1} can be assigned to the C–O stretching in OA.[42] The band at 1462 cm^{-1} is related to the $-CH=CH-$ structure in the OA molecule, and the signal shows a blue-shift to 1430 cm^{-1} in the Fe_3O_4@OA sample, confirming the coating of OA ligands on the surface of Fe_3O_4 nanoparticles. After heat treatment, the characteristic peaks corresponding to OA molecules disappeared in Fe_3O_4@OLCs, suggesting that OA has been transformed into graphitic shells.

A high-resolution TEM (HR-TEM) image (Fig. 3a) shows a measurement of the interlayer distance of ~0.25 nm, corresponding to the (311) crystal plane of a 5.6 nm inverse-spinel type Fe_3O_4 nanoparticles with high crystallinity. The TEM image of the Fe_3O_4@OLC (Fig. 3b) shows that Fe_3O_4 nanoparticles are tightly encapsulated in the covalently interconnected graphitic shells with the good particle size uniformity well-preserved, forming a three-dimensional Fe_3O_4@OLC framework. The graphitic framework has rather thin shell

thickness with an average 2–3 graphitic layers, which were derived from the *in situ* transformation of monolayer OA ligands. As shown in Fig. 3c, after insufficient acid etching, the Fe_3O_4 nanoparticles in the outside region of the hybrid structure were removed, leaving the cavities, while large amounts of Fe_3O_4 nanoparticles in the inside region of the hybrid structure were still encapsulated by OLCs. Relative OLC contents in both Fe_3O_4@OLCs and insufficiently etched Fe_3O_4@OLCs were determined by TG analysis. The results show that the weight loss of the hybrid structure occurs at ~400 °C in air (Fig. S1†), which is attributed to carbon burning. The relative carbon contents in the hybrid structures, corresponding to the weight losses within the temperature range of 400–620 °C, are found to be 38.1 wt% and 57.5 wt% in Fe_3O_4@OLCs and insufficiently etched Fe_3O_4@OLCs, respectively.

According to Brunauer–Emmett–Teller (BET) measurement (Fig. 3d), the Fe_3O_4@OLCs and insufficiently etched Fe_3O_4@OLCs exhibit hybrid I/IV-type N_2 adsorption/desorption curves. The increase of gas adsorption in the low pressure region and the adsorption hysteresis loop in the high pressure region indicate the presence of micropores and mesopores in the hybrid structure. The pore size measurements (Fig. 3e) show that the interconnected Fe_3O_4@OLCs and insufficiently etched interconnected Fe_3O_4@OLCs both have hierarchically porous structures with micropores mainly located at 1–1.5 nm and mesopores ranging from 2.5 to 25 nm. For Fe_3O_4@OLCs, the formation of large-sized mesopores is attributed to the
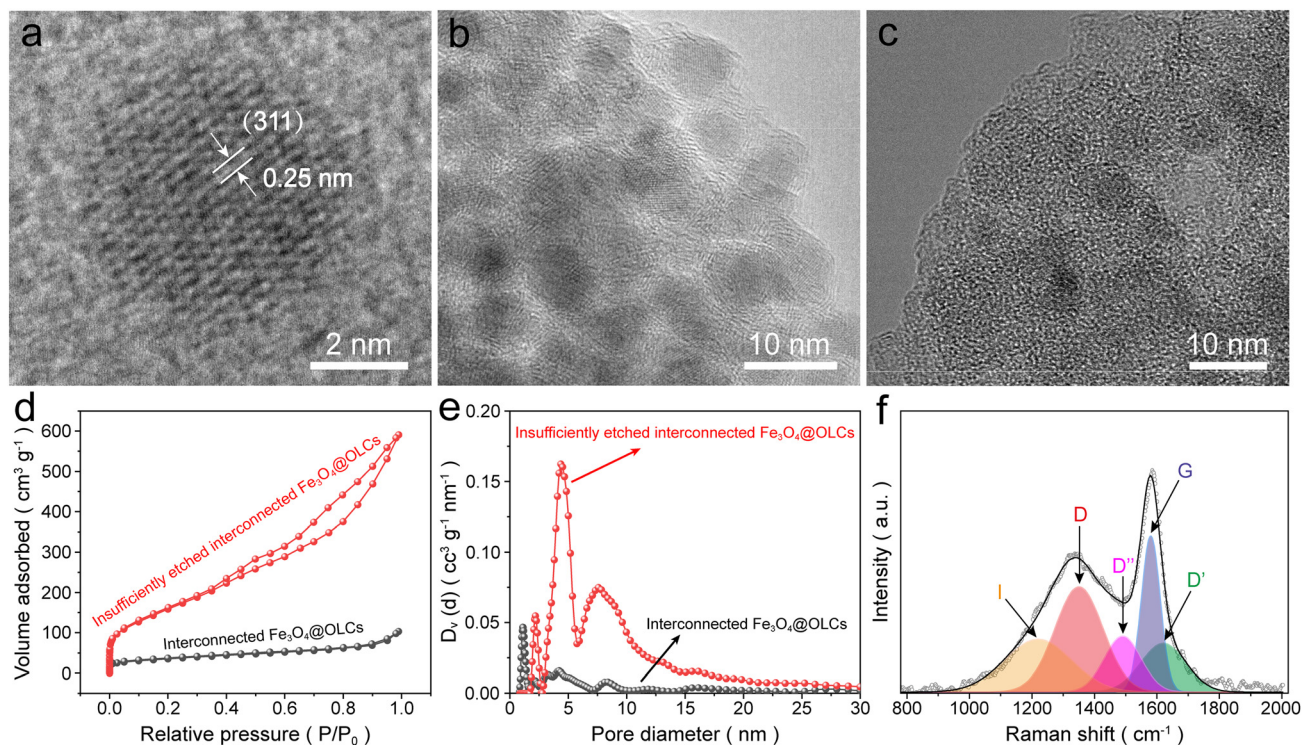
Fig. 3 (a) HR-TEM image of a Fe_3O_4@OA nanoparticle. TEM image of (b) interconnected Fe_3O_4@OLCs and (c) insufficiently etched interconnected Fe_3O_4@OLCs. (d) N_2 adsorption/desorption isotherms and (e) pore size distribution measurements of interconnected Fe_3O_4@OLCs and insufficiently etched interconnected Fe_3O_4@OLCs. (f) Raman spectra of insufficiently etched interconnected Fe_3O_4@OLCs.

stacking of Fe_3O_4@OLC particles, and the micropores and smaller-sized mesopores are mainly derived from the defects on graphitic layers and the exhausted pores generated during the thermal decomposition of OA. After insufficient acid etching, the pore volume at ~5 nm is substantially increased, matching the average size of Fe_3O_4 nanoparticles, which demonstrates that this pore volume increase is due to the removal of Fe_3O_4 nanoparticles. The increased pore volume at ~8 nm could be due to the amalgamation of smaller pores during the acid etching. The specific surface area of Fe_3O_4@OLCs is found to be 133.93 m^2 g^{-1}, which is dramatically increased to 576.8 m^2 g^{-1} after insufficient acid etching, higher than those of other reported magnetic adsorbents such as γ-Fe_2O_3/SiO_2 (74.3 m^2 g^{-1}),[43] Fe_3O_4/pine sawdust biochar (125.8 m^2 g^{-1}),[44] and Fe_3O_4@polydopamine@MOF (100.9 m^2 g^{-1}).[45] The high specific surface area of the hybrid structure is beneficial for adsorbing large amounts of organic dyes.

Raman spectroscopy (Fig. 3f) was also performed to evaluate the defect level of the insufficiently etched interconnected Fe_3O_4@OLCs. The D band at 1350 cm^{-1} arises from the structural defects and sp3-hybridized carbon, and the G band at 1580 cm^{-1} is caused by the sp2-hybridized graphitic carbons. The further deconvoluted peak signals at 1620 cm^{-1} and 1490 cm^{-1} are caused by the stacking disorder of graphene layers. The peak signal at 1220 cm^{-1} is attributed to the impurity elements, which is herein related to the presence of the inner Fe_3O_4 nanoparticles and oxygen species from the incomplete pyrolysis of OA. The presence of abundant defects in the insufficiently etched interconnected Fe_3O_4@OLC hybrid structure is confirmed by the intensity ratio of D to G bands (I_D/I_G) of 1.17, which is comparable to those of reported carbon-based adsorbents.[46] In addition, the magnetic hysteresis loop (Fig. S2†) demonstrates a ferromagnetic behavior in the insufficiently etched interconnected Fe_3O_4@OLC hybrid structure. Due to the large proportion of magnetic Fe_3O_4 nanoparticles presented in the hybrid structure, the uniform size distribution and ultrasmall size of Fe_3O_4 nanoparticles, and ultrathin graphitic coatings, the insufficiently etched interconnected Fe_3O_4@OLC hybrid structure exhibits a saturated magnetization of 36.8 emu g^{-1}. The saturated magnetism of insufficiently etched interconnected Fe_3O_4@OLCs is higher than those of reported carbon-coated Fe_3O_4 magnetic adsorbents,[24,26] which is mainly ascribed to the fact that the OLC shell of insufficiently etched interconnected Fe_3O_4@OLCs has an ultra-thin thickness, which minimizes the suppression of magnetism of the internal Fe_3O_4. The high saturated magnetism of insufficiently etched interconnected Fe_3O_4@OLCs corresponds to the high magnetic separation efficiency.[47] These imply that insufficiently etched interconnected Fe_3O_4@OLCs can move in a controllable manner in the external magnetic field, which is favorable for their efficient separation in the treated water.

The elemental states of the insufficiently etched interconnected Fe_3O_4@OLCs were further investigated by X-ray photoelectron spectroscopy (XPS). The full-survey spectrum shows the presence of three elements Fe, C, and O, indicating the presence of the remnant inner Fe_3O_4 nanoparticles (Fig. 4a). In the high-resolution spectrum, the Fe 2p signal (Fig. 4b) can

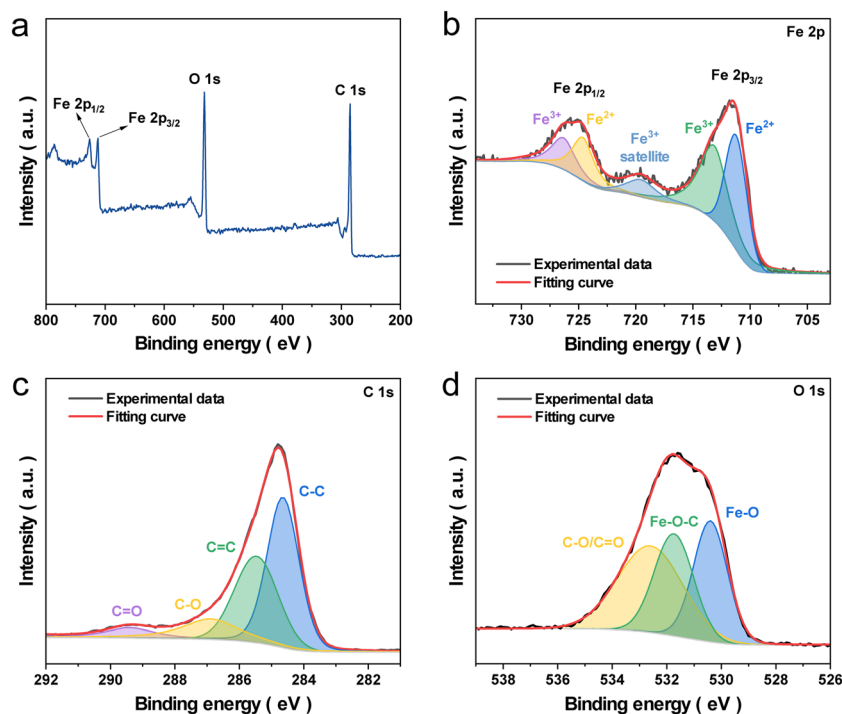**Fig. 4** (a) Full survey XPS spectrum of the insufficiently etched interconnected Fe_3O_4@OLCs. High-resolution XPS spectra of (b) Fe 2p, (c) C 1s, and (d) O 1s.

be assigned to two characteristic peaks at 711.7 eV and 725.2 eV, corresponding to Fe 2p3/2 and Fe 2p1/2, respectively. Due to the existence of two valence states of Fe atoms in Fe_3O_4, Fe 2p3/2 and Fe 2p1/2 can be further deconvoluted into four peaks, which are peaks at 713.2 eV and 726.4 eV attributed to Fe^{3+}, and peaks at 711.3 eV and 724.6 eV attributed to Fe^{2+}.[48] In the C 1s signal (Fig. 4c), the peaks at 284.6 eV, 285.5 eV, 286.9 eV and 289.3 eV are attributed to C–C, C=C, C–O and C=O, respectively. In the O 1s spectrum (Fig. 4d), the peak at 530.1 eV is attributed to the Fe–O bond originating from Fe_3O_4, while the peak at 532.7 eV assigned to C–O/C=O indicates the presence of oxygen-containing functional groups in the graphitic shells, which is formed from the incomplete decomposition of OA groups in Fe_3O_4@OA during thermal treatment. The peak at 531.6 eV corresponds to Fe–O–C bonding, confirming that the residual Fe_3O_4 core is tightly encapsulated by the OLC shells through covalent bonding between the two components.[48,49]

The dynamic adsorption process of MB on the insufficiently etched interconnected Fe_3O_4@OLC adsorbent was studied by UV-vis spectroscopy (Fig. 5a). With increasing adsorption time, the intensity of the absorption peak of MB at 665 nm decreased, corresponding to the decrease of MB concentration due to the increased adsorption on insufficiently etched interconnected Fe_3O_4@OLCs. After 90 min adsorption, the charac-

teristic peak nearly disappeared, indicating that MB was completely removed from water by the adsorbent. As shown in the inset in Fig. 5a, the insufficiently etched interconnected Fe_3O_4@OLC adsorbent after dye adsorption can be efficiently separated from the treated water in an external magnetic field. The high saturated magnetism and interconnected 3D graphitic framework are responsible for the efficient separation of the entire carbon structure. Fig. 5b shows the FT-IR spectra of MB, insufficiently etched interconnected Fe_3O_4@OLCs, and insufficiently etched interconnected Fe_3O_4@OLCs after MB adsorption (labeled as insufficiently etched interconnected Fe_3O_4@OLCs-MB). The characteristic absorbance band at 3435 cm^{-1} is ascribed to the –OH stretching vibrations for hydration. The bands at 2924 cm^{-1} and 2854 cm^{-1} can be assigned to the asymmetric and symmetric –CH_2 stretching, respectively. The band at 2345 cm^{-1} originated from C–H stretching, and the band at 1623 cm^{-1} is ascribed to C=O stretching. The bands at 1385 cm^{-1} (C–O–H bending vibration) and 1110 cm^{-1} (C–O vibration) indicate the presence of residual oxygen-containing functional groups in Fe_3O_4@OLCs. The peak at 877 cm^{-1} is derived from the out-of-plane bending vibration of C–H. The band at 593 cm^{-1} corresponds to the vibration of Fe–O. Compared to the sample before adsorption, the insufficiently etched interconnected Fe_3O_4@OLCs-MB exhibits weaker peak intensities at 1623 cm^{-1} (C=O), 1385 cm^{-1}
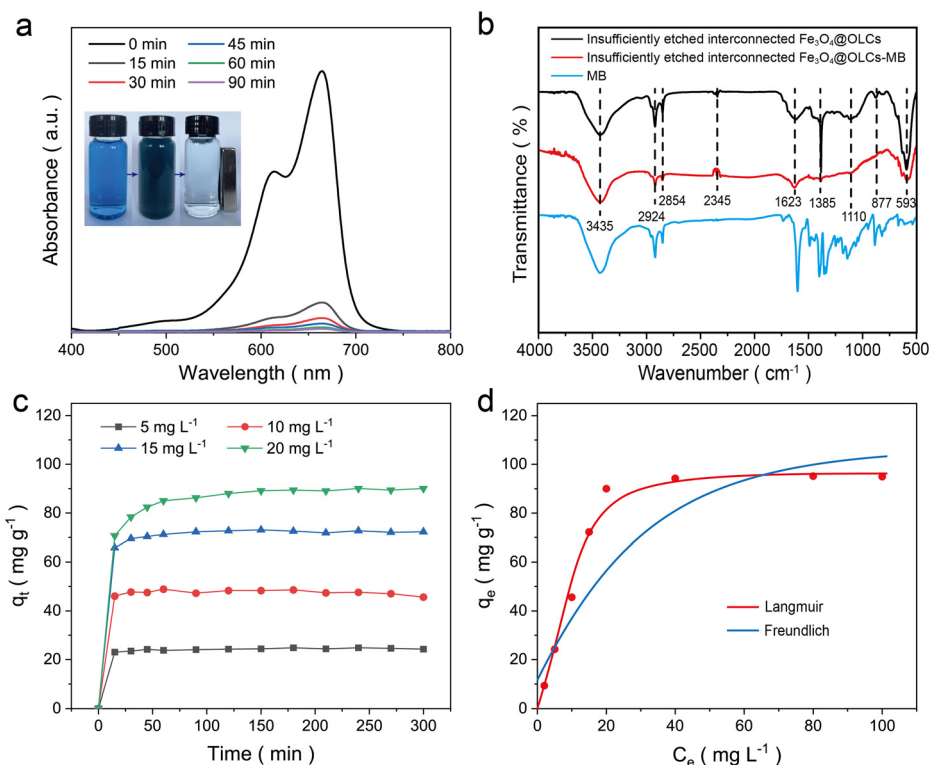
Fig. 5 (a) UV-vis spectra for the MB aqueous solutions (15 mg L^{-1}) treated with insufficiently etched interconnected Fe_3O_4@OLC adsorbents for different adsorption periods. Insets show the photograph of the insufficiently etched interconnected Fe_3O_4@OLCs in MB solution before and after magnetic separation. (b) FT-IR spectra of MB, insufficiently etched interconnected Fe_3O_4@OLCs, and insufficiently etched interconnected Fe_3O_4@OLCs-MB. (c) Variation of the adsorption capacities of insufficiently etched Fe_3O_4@OLCs with the treatment period. (d) Adsorption isotherms of MB.

(C–O–H) and 1110 cm^{-1} (C–O), suggesting MB adsorption on the surface. The oxygen-containing functional groups (C=O, C–O–H, and C–O) on the surface of insufficiently etched interconnected Fe$_3$O$_4$@OLCs are negatively charged in the aqueous environment, and can serve as the main adsorption sites for capturing and immobilizing the cationic dyes (MB) through electrostatic interactions. N and N–CH$_3$ in the MB ring can also form hydrogen bonds with oxygen-containing functional groups, which can suppress their stretching vibrations. Moreover, the highly positive surface curvature of the Fe$_3$O$_4$@OLCs enables the accommodation of high ion density on the surface.[50]

The adsorption performance of insufficiently etched interconnected Fe$_3$O$_4$@OLCs was studied in MB solutions with different concentrations of 5, 10, 15 and 20 mg L^{-1} (Fig. 5c). A rapid adsorption process was achieved within 30 min. All the samples reached the adsorption equilibrium and saturated adsorption amount in MB aqueous solution with different concentrations after 60 min, as demonstrated by the nearly zero slope of the adsorption–time curves. After 200 min, the insufficiently etched interconnected Fe$_3$O$_4$@OLCs exhibit a maximum adsorption capacity (q_t) of 90.2 mg g^{-1} in the MB solution with a concentration of 20 mg L^{-1}, which is superior to those of other reported magnetic adsorbents such as Fe$_3$O$_4$-magnetic activated carbon (32.25 mg g^{-1}),[51] MWCNTs/Fe$_3$O$_4$ (20.37 mg g^{-1}),[52] and Fe encapsulated magnetic carbon gels (67.75 mg g^{-1}).[53]

Due to the presence of Fe$_3$O$_4$, both interconnected Fe$_3$O$_4$@OLCs and insufficiently etched interconnected Fe$_3$O$_4$@OLCs can be easily separated from wastewater under a magnetic field after MB adsorption. However, the Fe$_3$O$_4$ nanoparticles in interconnected Fe$_3$O$_4$@OLCs before etching contribute to a large amount of "dead mass" during adsorption, leading to a saturation adsorption capacity of 68.7 mg g^{-1} after 90 min (Fig. S3†). In contrast, insufficiently etched interconnected Fe$_3$O$_4$@OLCs expose more pores due to the partial removal of Fe$_3$O$_4$, generating a higher specific surface area while maintaining magnetism. As a result, Fe$_3$O$_4$@OLCs exhibit a saturation adsorption capacity of 90.2 mg g^{-1} after only 60 min (Fig. 5c). This improved adsorption performance is mainly attributed to the increased permeability of MB molecules in insufficiently etched interconnected Fe$_3$O$_4$@OLCs.

As shown in Fig. S4,† there is no sufficient space for MB adsorption in the inside region of interconnected Fe$_3$O$_4$@OLCs due to the dense packing of Fe$_3$O$_4$ nanoparticles, hindering the penetration of MB molecules. Consequently, MB is adsorbed mainly on the surface regions, resulting in a lower adsorption capacity and rate. After HCl etching, insufficiently etched interconnected Fe$_3$O$_4$@OLCs provide more pores and cavities in the inside region (Fig. 5c), allowing MB molecules to penetrate into the interconnected OLC structure and leading to a higher adsorption capacity. Additionally, according to TG measurements (Fig. S1†), the OLC mass ratio in insufficiently etched interconnected Fe$_3$O$_4$@OLCs is 57.5%, higher than 38.1% in Fe$_3$O$_4$@OLCs, which is also beneficial for its higher adsorption capacity.

The adsorption mechanism was investigated using equilibrium adsorption isotherms (Fig. 5d). The adsorption capacity of insufficiently etched interconnected Fe$_3$O$_4$@OLCs increased with increasing dye concentration. The isotherm shows an L-behavior adsorption feature, suggesting a high affinity between Fe$_3$O$_4$@OLCs and MB molecules.[54] When the MB concentration is low, Fe$_3$O$_4$@OLCs can provide plenty of active sites to allow for a rapid adsorption, exhibiting a steep slope of the isotherm. As the MB concentration is increased, the adsorption becomes more difficult due to the decrease of adsorption sites, especially when the saturated adsorption is reached.[55] The experimental equilibrium adsorption isotherm can be well fitted with the Langmuir model with an R_2 = 0.97323 (Fig. 5d) rather than the Freundlich model (corresponding to the multilayer adsorption process), demonstrating a monolayer adsorption behavior of MB, which results in a fast adsorption rate between MB molecules and insufficiently etched interconnected Fe$_3$O$_4$@OLCs. The adsorption kinetics behavior is consistent with those of other reported carbon-based adsorbents.[54,56] The ultrathin and defective graphitic coatings enable a high specific surface area and abundant pore structures in the insufficiently etched interconnected Fe$_3$O$_4$@OLCs for adsorption. The 3D covalently interconnected graphitic coating framework and the tight encapsulation of inner Fe$_3$O$_4$ nanoparticles result in rapid moving of the entire hybrid structure in the magnetic field. These advantages bestowed the insufficiently etched interconnected Fe$_3$O$_4$@OLCs with high adsorption capacity, efficient separation from treated water and good recyclability for adsorbent applications.

The isolated adsorbents loaded with organic dyes are often treated as solid waste, thus presenting a potential risk of secondary environmental pollution. Eco-friendly treatment of solid waste to form high-value-added products can realize the cascaded utilization of adsorbents and reduce the environmental pollution. In this study, the insufficiently etched interconnected Fe$_3$O$_4$@OLCs saturated with MB dyes were converted into an N-doped hollow onion-like carbon (N-doped HOLC) material through thermal treatment at 850 °C, which is used as a supercapacitor electrode material. As shown in Fig. 6a, the obtained N-doped HOLCs maintain a three-dimensional interconnected structure of a circular hollow carbon unit. HR-TEM images also show a short-range ordered state of the carbon layer (Fig. 6b), and the discontinuous characteristics of the carbon layer stripes correspond to a large number of defects and pore structures. The XRD result of the N-doped HOLCs shows two broad diffraction peaks at ~26.2° and ~42.7° (Fig. S5†), corresponding to the (002) and (100) planes of the graphitic structure, respectively. This indicates a partially graphitized structure formed during pyrolysis, which is beneficial for enhacing the conductivity of the OLC structure. The measurement results of the pore size distribution of N-doped HOLCs are shown in Fig. 6c, where micropores with a size of ~2 nm and mesopores with a size of ~5 nm account for the largest proportion. The mesopores are mainly derived from the hollow structure and stacking gaps of the N-doped HOLCs
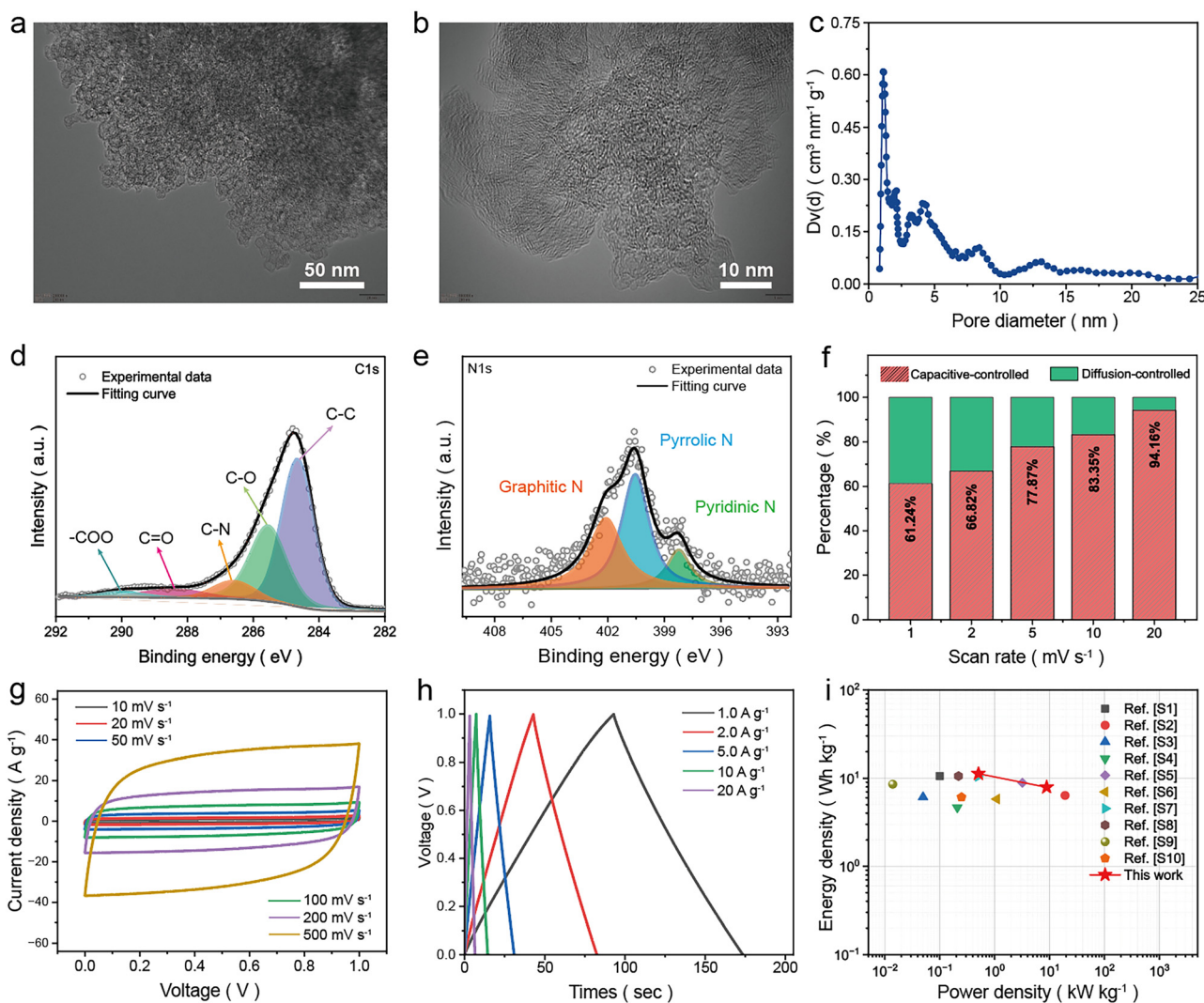
Fig. 6 Structural characterization and energy storage performance evaluation of N-doped HOLCs. (a) TEM and (b) HR-TEM images of N-doped HOLCs. (c) Pore size distribution measurements of N-doped HOLCs. High-resolution XPS spectrum of N-doped HOLCs: (d) C 1s and (e) N 1s. (f) Contribution ratios of the capacitive-controlled process at different scan rates from 1 to 20 mV s^{-1}. (g) CV curves of the symmetric supercapacitor based on N-doped HOLCs at different scan rates from 10 to 500 mV s^{-1}. (h) GCD curves of the symmetric supercapacitor at current densities from 1 to 20 A g^{-1}. (i) Ragone plot comparing the energy and power density of the supercapacitor based on N-doped HOLCs with other supercapacitive materials.

after the removal of Fe_3O_4 nanoparticles. The micropores are mainly derived from the non-graphitization defects of the N-doped HOLCs. Appropriate mesopores are conducive to the efficient transport of electrolyte ions, while micropores can directly increase the ion storage capacity.

Fig. 6d and e show the XPS results of the converted N-doped HOLC material. The peaks at 284.7 eV, 285.6 eV, 288.4 eV, and 289.9 eV in the C 1s spectrum (Fig. 6d) are associated with C–C, C–O, C=O, and ester (–COO) groups, respectively. The peak at 286.6 eV corresponds to the C–N group, which indicates that N atoms have been doped into the carbon structure during thermal treatment. The N 1s spectrum (Fig. 6e) revealed a total N atomic content of ~5%, with the peaks located at 398.8 eV, 400.5 eV, and 402.3 eV assigned to

graphitic N, pyrrolic N, and pyridinic N, respectively. The different types of N atoms can not only improve the conductivity and wettability of the carbon materials, but also introduce additional pseudocapacitive contributions for supercapacitive energy storage. Cyclic voltammetry (CV) measurements were performed on N-doped HOLCs and insufficiently etched interconnected Fe_3O_4@OLCs in a three-electrode testing system to evaluate their electrochemical energy storage performances (Fig. S6†). The quasi-rectangular shapes of CV curves indicate typical supercapacitive electrochemical processes. The N-doped HOLCs exhibit a larger area of the CV curve than insufficiently etched interconnected Fe_3O_4@OLCs, implying higher electrochemical activity. As shown in Fig. S6c and S6d,† the N-doped HOLCs exhibit a gravimetric specific

capacitance of 176.1 F g^{-1} at a scan rate of 5 mV s^{-1}, which is higher than that of the insufficiently etched interconnected Fe$_3$O$_4$@OLCs of 110.3 F g^{-1}. The improvement in energy storage performance can be attributed to the improved conductivity due to the increased graphitic crystallinity after thermal treatment and the presence of graphitic N atoms, enhanced wettability due to N doping, as well as the increased pseudocapacitive electrochemical behavior originating from the pyrrolic N.

N-Doping typically increases the redox-active sites in carbon-based electrode materials, introducing a pseudocapacitive energy storage process. Calculations of contributions from different energy storage mechanisms (Fig. 6f and Fig. S7†) show that the capacitive-controlled process increased from 61.24% to 94.16% on increasing the scan rates ranging from 1 to 20 mV s^{-1}, confirming that N-doped HOLCs are an EDLC-predominated supercapacitor electrode material. The EDLC-dominated behavior endows the N-doped HOLCs with the advantage of high power, while the pseudocapacitance induced by N-doping enhances the energy density by enabling the faradaic process.

A symmetric supercapacitor was assembled based on the N-doped HOLCs. CV curves at scan rates ranging from 10 to 500 mV s^{-1} (Fig. 6g) do not exhibit obvious distortions with increasing scan rates, indicating fast ion and electron transportation within the electrode structure. In Fig. S8,† the electrochemical impedance spectroscopy (EIS) spectrum reveals a smaller semicircle radius and a shorter Warburg diffusion segment in the mid-frequency area, indicating a rapid electrochemical response behavior.[57] Moreover, the supercapacitor shows low equivalent series resistance (R_s) and charge transfer resistance (R_{ct}) values of 2.4 Ω and 0.8 Ω, respectively, which demonstrates an efficient electronic transfer and ion diffusion within the electrode material. Galvanostatic charge–discharge (GCD) curves (Fig. 6h) of the supercapacitor display quasi-symmetric-trianglular shapes, which confirms the surface capacitive storage behaviors of the N-doped HOLCs. A voltage drop of only 0.01 V is measured at a current density of 1 A g^{-1}, which is attributed to its excellent conductivity. As shown in Fig. S9,† the supercapacitor exhibits a specific capacitance of up to 81.5 F g^{-1} at a current density of 1 A g^{-1}, and when the test current density increases to 20 A g^{-1}, the specific capacitance of the device becomes 72.4 F g^{-1}. After a 20-fold increase in the charge–discharge current, the device exhibits a capacitance retention rate of up to 88.8% corresponding to its good rate performance.

Moreover, the electrochemical cycling stability of the supercapacitor was also studied. As shown in Fig. S10,† a high capacitance retention of 94.6% is achieved after 10 000 GCD cycles at a current density of 10 A g^{-1}. The supercapacitor based on N-doped HOLCs exhibits a maximum energy density of 11.3 W h kg^{-1} at a power density of 0.51 kW kg^{-1} and a current density of 1 A g^{-1} (Fig. 6i). Moreover, a maximum power density of 8.9 kW kg^{-1} along with an energy density of 7.9 W h kg^{-1} were obtained at a current density of 20 A g^{-1}. These exceeded those of reported carbon-based supercapacitor materials (listed in Table S1†), such as quinone-decorated onion-like carbon (6.4 W h kg^{-1}),[58] HPCF (9.1 W h kg^{-1}),[59] and N–C–HPCS (6.1 W h kg^{-1}).[60] Fig. S11† shows a proof-demonstration of three supercapacitors connected in series, which can power 27 LED beads, suggesting their potential application as power sources for energy storage.

4. Conclusions

In summary, we realized a cascaded utilization of an insufficiently etched interconnected Fe$_3$O$_4$@OLC hybrid structure in wastewater treatment and supercapacitive energy storage. The hybrid structure was synthesized by carbonizing monodisperse Fe$_3$O$_4$@OA colloidal nanocrystals and subsequent incomplete removal of inner Fe$_3$O$_4$ nanoparticles by short-period acid etching. The hybrid structure possesses hollow OLCs in the outside region and Fe$_3$O$_4$@OLCs with ultrathin graphitic coatings in the inside region. The graphitic layers are covalently interconnected in three dimensions in the whole structure. As a result, it simultaneously exhibits a high specific surface area of 576.8 m^2 g^{-1} and a high saturated ferromagnetism. These synergistically render the insufficiently etched interconnected Fe$_3$O$_4$@OLCs with a high adsorption capacity of 90.2 mg g^{-1} in the MB aqueous solution, good preservation of ferromagnetism and efficient separation from treated water in an external magnetic field. The MB-adsorbed insufficiently etched interconnected Fe$_3$O$_4$@OLC waste product was thermally transformed into N-doped HOLCs as electrode materials for supercapacitor applications. The electrode exhibits a high specific capacitance of 176.1 F g^{-1}, and the assembled symmetric supercapacitor possesses a high electrochemical cycling stability with a high capacitance retention of 94.6% after 10 000 GCD cycles. Interconnected graphitic layers and heteroatom N doping are responsible for the high energy storage performances. This study demonstrates a cascaded utilization of the Fe$_3$O$_4$@OLC hybrid structure for organic dye adsorption and supercapacitive energy storage, which provides a design and synthesis strategy for functional carbon nanostructures for cascaded and sustainable utilization in environmental and energy storage applications.

Author contributions

Xin Jiao: Conceptualization, investigation, methodology, and writing – original draft. Min Xiao: Data curation, investigation, methodology, and validation. Fengshi Cai: Methodology and writing – review & editing. Yingchun Fan: Formal analysis, investigation, and writing – original draft. Shuaipeng Meng: Investigation and methodology. Xiude Guan: Investigation and methodology. Huiquan Wang: Investigation and methodology. Chenguang Zhang: Project administration, supervision, conceptualization, funding acquisition, and writing – review & editing.

Data availability

The data supporting this article have been included as part of the ESI.†

Conflicts of interest

The authors declare that they have no known competing financial interests or personal relationships that could have appeared to influence the work reported in this paper.

Acknowledgements

References

1 W. Dong, H. Xiao, Y. Jia, L. Chen, H. Geng, S. U. H. Bakhtiar, Q. Fu and Y. Guo, *Adv. Sci.*, 2022, **9**, 2105368.

2 W. Mellor, E. Wright, R. Clift, A. Azapagic and G. Stevens, *Chem. Eng. J.*, 2022, **57**, 4697–4713.

3 D. Mallesh, J. Anbarasan, P. Mahesh Kumar, K. Upendar, P. Chandrashekar, B. V. S. K. Rao and N. Lingaiah, *Appl. Surf. Sci.*, 2020, **530**, 147226.

4 M. Kalverkamp, A. Pehlken and T. Wuest, *Sustainability*, 2017, **9**, 1540.

5 Y. Ma, J. Wei, J. Zhu, Y. Hu, Y. Cai, J. Zheng and H. Fan, *Appl. Surf. Sci.*, 2023, **639**, 158238.

6 J. Yang, H. Wang, Y. Yang, J. Wu, P. Hu and L. Guo, *Nanoscale*, 2017, **9**, 9879–9885.

7 A. A. Elhakim, M. El-Kemary, M. M. Ibrahim, I. M. El-Mehasseb and H. S. El-Sheshtawy, *Appl. Surf. Sci.*, 2021, **564**, 150410.

8 A. H. Jawad and A. S. Abdulhameed, *Surf. Interfaces*, 2020, **18**, 100422.

9 C. Liu, A. M. Omer and X. K. Ouyang, *Int. J. Biol. Macromol.*, 2018, **106**, 823–833.

10 A. V. Baskar, N. Bolan, S. Hoang, P. Sooriyakumar, M. Kumar, L. Singh, T. Jasemizad, L. P. Padhye, G. Singh, A. Vinu, B. Sarkar, M. B. Kirkham, J. Rinklebe, S. Wang, H. Wang, R. Balasubramanian and K. H. M. Siddique, *Sci. Total Environ.*, 2022, **822**, 153555.

11 D. Yu, H. Wang, J. Yang, Z. Niu, H. Lu, Y. Yang, L. Cheng and L. Guo, *ACS Appl. Mater. Interfaces*, 2017, **9**, 21298–21306.

12 J. Yang, Y. Yang, A. Li, Z. Wang, H. Wang, D. Yu, P. Hu, M. Qian, J. Lin and L. Guo, *Energy Storage Mater.*, 2019, **17**, 334–340.

13 E. Da'na and A. Awad, *J. Environ. Chem. Eng.*, 2017, **5**, 3091–3099.

14 S. Matsuda, A. R. Durney, L. He and H. Mukaibo, *Bioresour. Technol.*, 2016, **200**, 914–920.

15 H.-X. Zhao, M.-X. Li, Y. Wang, Y.-Z. Tan, Z.-X. Zhou, Y.-R. Guo and Q.-Z. Pan, *Appl. Surf. Sci.*, 2024, **646**, 158936.

16 J. F. Liu, Z. S. Zhao and G. B. Jiang, *Environ. Sci. Technol.*, 2008, **42**, 6949–6954.

17 L. Wang, F. Liu, A. Pal, Y. Ning, Z. Wang, B. Zhao, R. Bradley and W. Wu, *Carbon*, 2021, **179**, 327–336.

18 Y. Liu, W. Jiang, S. Li and F. Li, *Appl. Surf. Sci.*, 2009, **255**, 7999–8002.

19 H.-S. Jeong, H. Kim, K.-I. Jo, J. Jang, J.-H. Choi and J. Koo, *Appl. Surf. Sci.*, 2020, **508**, 144416.

20 M. Moztahida, J. Jang, M. Nawaz, S. R. Lim and D. S. Lee, *Sci. Total Environ.*, 2019, **667**, 741–750.

21 X. Liu, J. Tian, Y. Li, N. Sun, S. Mi, Y. Xie and Z. Chen, *J. Hazard. Mater.*, 2019, **373**, 397–407.

22 M. A. Farghali, R. M. El Bahnasawy and T. A. Salaheldin, *Inorg. Chem. Commun.*, 2021, **132**, 108823.

23 H. A. Pereira, K. da Boit Martinello, Y. Vieira, J. C. Diel, M. S. Netto, G. D. Reske, E. Lorenzett, L. F. O. Silva, T. A. L. Burgo and G. L. Dotto, *Chemosphere*, 2023, **325**, 138384.

24 H. Pan, X. Jiao, W. Zhang, L. Fan, Z. Yuan and C. Zhang, *Chem. Eng. J.*, 2024, **484**, 149663.

25 H. V. Tran, O. T. K. Do, N. D. Nguyen and C. D. Huynh, *New J. Chem.*, 2022, **46**, 10644–10651.

26 L. Zhou, G. Zhang, J. Tian, D. Wang, D. Cai and Z. Wu, *ACS Sustainable Chem. Eng.*, 2017, **5**, 11042–11050.

27 X. Sun, A. Zhou, S. Li and M. Li, *ACS Appl. Nano Mater.*, 2021, **4**, 13655–13663.

28 M. Haris, A. Zavabeti, M. W. Khan, B. J. Murdoch, J. Paz-Ferreiro, N. Mahmood and N. Eshtiaghi, *J. Environ. Chem. Eng.*, 2022, **10**, 108968.

29 H. Lan, S. Zhang, J. Zhang, Y. Cui, Q. Tang, X. An, H. Liu and J. Qu, *Appl. Surf. Sci.*, 2023, **614**, 156172.

30 M. Vakili, S. Deng, G. Cagnetta, W. Wang, P. Meng, D. Liu and G. Yu, *Sep. Purif. Technol.*, 2019, **224**, 373–387.

31 S. Y. Hwang, G. B. Lee, J. H. Kim, B. U. Hong and J. E. Park, *Molecules*, 2020, **25**, 4561.

32 D. Jiang, B. Chu, Y. Amano and M. Machida, *Colloids Surf., A*, 2018, **558**, 429–437.

33 X. N. Zhang, G. Y. Mao, Y. B. Jiao, Y. Shang and R. P. Han, *Int. J. Environ. Sci. Technol.*, 2014, **11**, 1439–1448.

34 M. Shahadat and S. Isamil, *RSC Adv.*, 2018, **8**, 24571–24587.

35 V. Acevedo-García, E. Rosales, A. Puga, M. Pazos and M. A. Sanromán, *Sep. Purif. Technol.*, 2020, **242**, 116796.

36 V. Abromaitis, V. Racys, P. Van Der Marel and R. J. Meulepas, *Chemosphere*, 2016, **149**, 183–189.

37 L. Fan, C. Mao, H. Wang and C. Zhang, *ACS Appl. Nano Mater.*, 2024, **7**, 20954–20963.

38 S. G. Kwon, Y. Piao, J. Park, S. Angappane, Y. Jo, N. M. Hwang, J. G. Park and T. Hyeon, *J. Am. Chem. Soc.*, 2007, **129**, 12571–12584.

39 D. Wang, P. Yang and Y. Zhu, *Mater. Res. Bull.*, 2014, **49**, 514–520.

40 R. D. Hunter, J. Ramírez-Rico and Z. Schnepp, *J. Mater. Chem. A*, 2022, **10**, 4489–4516.

41 L. Yu, Y. Tang, W. Ma, Y. Zhang, B. Zhang, L. Liu, S. Dong and S. Yan, *Appl. Surf. Sci.*, 2024, **653**, 159333.

42 F. Söderlind, H. Pedersen, R. M. Petoral, P. O. Käll and K. Uvdal, *J. Colloid Interface Sci.*, 2005, **288**, 140–148.

43 W. Zhang, L. Y. Zhang, X. J. Zhao and Z. Zhou, *J. Mol. Liq.*, 2016, **222**, 995–1002.

44 F. Reguyal, A. K. Sarmah and W. Gao, *J. Hazard. Mater.*, 2017, **321**, 868–878.

45 G. Zhou, Q. Wang, R. Song, S. Li, S. Yang and Q. Zhang, *J. Phys. Chem. Solids*, 2023, **172**, 111094.

46 Z. Yin, B. Shen, C. Cui, H. Chen, Duoni, J. Wang, W. Qian and L. Zhao, *ACS Appl. Mater. Interfaces*, 2021, **13**, 43266–43272.

47 C. Zhang, J. Li, C. Shi, C. He, E. Liu and N. Zhao, *Nano Res.*, 2016, **9**, 1159–1172.

48 X. Jiao, B. Li, J. Wang, Y. Fan, Y. Ma, Z. Yuan and C. Zhang, *Carbon*, 2023, **203**, 261–272.

49 H. Fan, R. Niu, J. Duan, W. Liu and W. Shen, *ACS Appl. Mater. Interfaces*, 2016, **8**, 19475–19483.

50 C. G. Zhang, H. Z. Du, K. Ma and Z. H. Yuan, *Adv. Energy Mater.*, 2020, **10**, 2002132.

51 D. R. Vaddi, R. Malla and S. Geddapu, *Desalin. Water Treat.*, 2024, **317**, 100146.

52 C. S. Lee, S. H. Shuit, G. G. Lim, Q. H. Ng, P. Y. Hoo, S. Lim and Y. P. Teoh, *J. Water Process Eng.*, 2022, **45**, 102487.

53 J. Bibin, I. A. Al-Omari, S. H. Al-Harthi, M. Manoj, K. C. Dhanyaprobha, M. T. Z. Myint and T. Hysen, *Int. J. Environ. Sci. Technol.*, 2023, **20**, 4779–4796.

54 C. H. Giles, T. H. Macewan, S. N. Nakhwa and D. Smith, *J. Chem. Soc.*, 1960, **56**, 1973–2993.

55 L. Ai, H. Huang, Z. Chen, X. Wei and J. Jiang, *Chem. Eng. J.*, 2010, **156**, 243–249.

56 J. Yang, Y. Dou, H. Yang and D. Wang, *Appl. Surf. Sci.*, 2021, **538**, 148110.

57 C. G. Zhang, X. Jiao, Y. Wang, K. Ma, Y. Zhou, Y. Ma and H. Wang, *Small*, 2023, **20**, 2305949.

58 M. Bhaumik, K. Raju, I. Arunachellan, T. Ludwig, M. K. Mathe, A. Maity and S. Mathur, *Electrochim. Acta*, 2020, **342**, 13611.

59 Y. Zhang, R. Shao, W. Xu, J. Ding, Y. Wang, X. Yan, W. Shi and M. Wang, *Chem. Eng. J.*, 2021, **419**, 129576.

60 S. Park, B. Seo, D. Shin, K. Kim and W. Choi, *Chem. Eng. J.*, 2022, **433**, 134486.